Journal of Medical Imaging

MedicalImaging.SPIEDigitalLibrary.org

7T MRI subthalamic nucleus atlas for use with 3T MRI

Mikhail Milchenko
Scott A. Norris
Kathleen Poston
Meghan C. Campbell
Mwiza Ushe
Joel S. Perlmutter
Abraham Z. Snyder

SPIE.

Mikhail Milchenko, Scott A. Norris, Kathleen Poston, Meghan C. Campbell, Mwiza Ushe, Joel S. Perlmutter, Abraham Z. Snyder, "7T MRI subthalamic nucleus atlas for use with 3T MRI," *J. Med. Imag.* **5**(1), 015002 (2018), doi: 10.1117/1.JMI.5.1.015002.

7T MRI subthalamic nucleus atlas for use with 3T MRI

Mikhail Milchenko,[a,*] Scott A. Norris,[b] Kathleen Poston,[c] Meghan C. Campbell,[b] Mwiza Ushe,[b] Joel S. Perlmutter,[b] and Abraham Z. Snyder[a,b]
[a]Washington University in St. Louis School of Medicine, Mallinckgrodt Institute of Radiology, St. Louis, Missouri, United States
[b]Washington University in St. Louis School of Medicine, Department of Neurology, St. Louis, Missouri, United States
[c]Stanford University Medical Center, Department of Neurology & Neurological Sciences, Palo Alto, California, United States

Abstract. Deep brain stimulation (DBS) of the subthalamic nucleus (STN) reduces motor symptoms in most patients with Parkinson disease (PD), yet may produce untoward effects. Investigation of DBS effects requires accurate localization of the STN, which can be difficult to identify on magnetic resonance images collected with clinically available 3T scanners. The goal of this study is to develop a high-quality STN atlas that can be applied to standard 3T images. We created a high-definition STN atlas derived from seven older participants imaged at 7T. This atlas was nonlinearly registered to a standard template representing 56 patients with PD imaged at 3T. This process required development of methodology for nonlinear multimodal image registration. We demonstrate mm-scale STN localization accuracy by comparison of our 3T atlas with a publicly available 7T atlas. We also demonstrate less agreement with an earlier histological atlas. STN localization error in the 56 patients imaged at 3T was less than 1 mm on average. Our methodology enables accurate STN localization in individuals imaged at 3T. The STN atlas and underlying 3T average template in MNI space are freely available to the research community. The image registration methodology developed in the course of this work may be generally applicable to other datasets. [DOI: 10.1117/1.JMI.5.1.015002]

Keywords: deep brain stimulation; subthalamic nucleus; Parkinson disease; image registration; atlas.

Paper 17141RR received May 17, 2017; accepted for publication Dec. 12, 2017; published online Jan. 8, 2018.

1 Introduction

Deep brain stimulation (DBS) of the subthalamic nucleus (STN) reduces motor symptoms in Parkinson disease (PD). Undesirable side effects include changes in mood and cognition.[1,2] Variability of stimulation site relative to the STN may account for inconsistent effects on movement, cognition, and mood.[3–7] Studying these effects requires accurate postoperative localization of electrodes relative to the STN, and this requires neuroimaging methods to precisely identify the STN.

Current imaging methods inadequately permit unambiguous identification of the STN in individual patients. Specifically, the STN cannot be directly identified in magnetic resonance images (MRIs) acquired with conventional 1.5T and 3T scanners because of insufficient contrast.[8] Two indirect strategies currently in clinical practice circumvent this limitation. First, the STN may be localized in relation to identifiable fiducials, e.g., the anterior commissure.[9] However, individual variability in STN anatomy and its relation to manually identified landmarks limit the accuracy of this approach. Alternatively, individual MRIs may be registered to a brain atlas in which the STN has been delineated.[10] Atlas-based localization eliminates subjectivity in the delineation of anatomical structures such as the STN. However, to be useful, the atlas must be well matched to the population being studied, i.e., patients with PD, since the contrast properties of the STN and its shape may be population-specific.

Yelnik et al.[11] developed an atlas based on MRIs in which they delineated the STN and basal ganglia using histological sections of the same patient. More recently, STN localization has been improved by exploiting T2* contrast;[12–14] this strategy is especially effective with high-field (7-Tesla) MRI, both *in vivo*[15–18] and *ex vivo*.[19] Several alternative atlases have been created but assessing the extent to which these atlases are consistent remains a challenge.[18,20–22]

Here, we address the above-described challenges by creating a high-definition STN atlas based on *in vivo* 7T MRI. The 7T images are linked by image registration to an averaged template representing patients with PD imaged at 3T. In brief, our strategy involves three steps: (1) a "probabilistic" STN atlas representing normal older individuals was generated using high-resolution 7T MRI;[23] (2) an average template was created using conventional 3T MRI acquired in a clinical PD population; and (3) the 7T and 3T results were mutually coregistered using a nonlinear registration technique. The same technique may be used to warp clinical MR images to the 3T template or to coregister alternative atlases. This registration method also estimates alignment accuracy at each locus.

2 Methods

2.1 *Imaging*

MRI data contributing to the present results were obtained in two cohorts scanned at Stanford University (SU) and at Washington University (WU). All studies were approved by the local Institutional Review Boards, all participants signed written informed consent, and data were deidentified prior to sharing.

*Address all correspondence to: Mikhail Milchenko, E-mail: mmilchenko@wustl.edu

2329-4302/2018/$25.00 © 2018 SPIE

2.1.1 *SU dataset*

Nine participants had imaging at the Stanford University Lucas Center using a GE 7T Discovery 950 whole-body MR scanner (GE Healthcare, Waukesha, Wisconsin) equipped with a 32-channel receiver coil and a quadrature transmit coil (Nova Medical Inc., Wilmington, Massachusetts). High contrast visualization of the STN, red nucleus (RN), and substantia nigra was obtained with a whole-brain, coronal, magnetization-prepared fluid-attenuated inversion recovery sequence (Cube T2-weighted FLAIR, field of view of 179 mm × 179 mm × 173 mm, acquisition matrix 224 × 224 × 216 reconstructed to 256 × 256 × 216, acquisition resolution 0.8 mm × 0.8 mm × 0.8 mm reconstructed to 0.7 mm × 0.7 mm × 0.8 mm, echo time = 109.5 ms, repetition time = 8000 ms, inversion time = 2135 ms, bandwidth 62.50 Hertz/pixel, scan time 5 min 24 s[23]). Each participant also had 3T T1-weighted FSPGR (fast spoiled gradient echo) scan on a GE Discovery MR750 scanner (General Electric, Milwaukee, Wisconsin) (TI 300 ms, TR 8.4 ms, TE 1.8 ms, flip angle 15 deg, 22 cm field of view, acquired resolution, 1.5 mm × 0.9 mm × 1.1 mm) to enable cross-modal registration of the T2-weighted 7T images. Data from two participants were excluded owing to ventriculomegaly or excessive head motion. Thus, the useable SU data set comprised seven normal participants (five female, age 66 ± 7 years).

2.1.2 *WU dataset*

At WU in St. Louis, a separate group of 56 (24 women) patients with PD (age 67 ± 6 years) had scans on a Siemens 3T MAGNETOM Trio scanner (Erlangen, Germany). Each patient had one T1-weighted scan (3D MP-RAGE, 0.9 mm cubic isotropic voxels, TR 2.4 s, TE 3.14 ms, inversion time 1 s, flip angle 8 deg) and one T2-weighted scan (3D SPACE, 0.9 mm cubic isotropic voxels, TR 3.2 s, TE = 461 ms, and flip angle = 120 deg).

2.2 *Spatial Alignment*

2.2.1 *Spatial registration algorithms*

We used a combination of affine and nonlinear transforms for all spatial registrations. Essential image registration schemes are presented in Fig. 1. Expanded methodological details are given in Appendix D. All transforms were computed using the conjugate metric gradient objective function [*cmg*; see Appendix A(a)]. We chose *cmg* as the voxel similarity measure as it works well for cross-modal registration.[24] Nonlinear warping was implemented using multiscale block matching [Appendix A(b)] to optimize the *cmg* measure (hence, *bm-cmg*). The rationale for developing *bm-cmg* is discussed below (see Sec. 4). In all registrations, affine transformation was used to initialize the nonlinear stage as this approach produces the best results for subcortical structures.[25] The *bm-cmg* algorithm automatically estimates the nonlinear registration error at each voxel [Appendix A(c)]; these values play a role in the selection of target images (see Appendix D). When applying a chain of transforms, we computed transform composition prior to resampling step, to eliminate the loss of spatial resolution. For example, to resample a T2-weighted image in atlas space, the relevant transform was computed as T2w → T1w → template, where the template is T1-weighted. All present resampling steps were computed using trilinear interpolation.

2.3 *Creating STN "Probabilistic" Atlas from SU 7T Images*

2.3.1 *Creating average template images*

T1w (SPGR) and T2w (MP-FLAIR) images from each participant were coregistered by means of rigid body transforms with six degrees of freedom (DOF) [Fig. 1(a)] for each of the seven SU participants. The participant with the best-defined STN was selected as the T2w warp target (SU_7T_T2w_t) for the remaining six participants. Registration of individual T2w images to

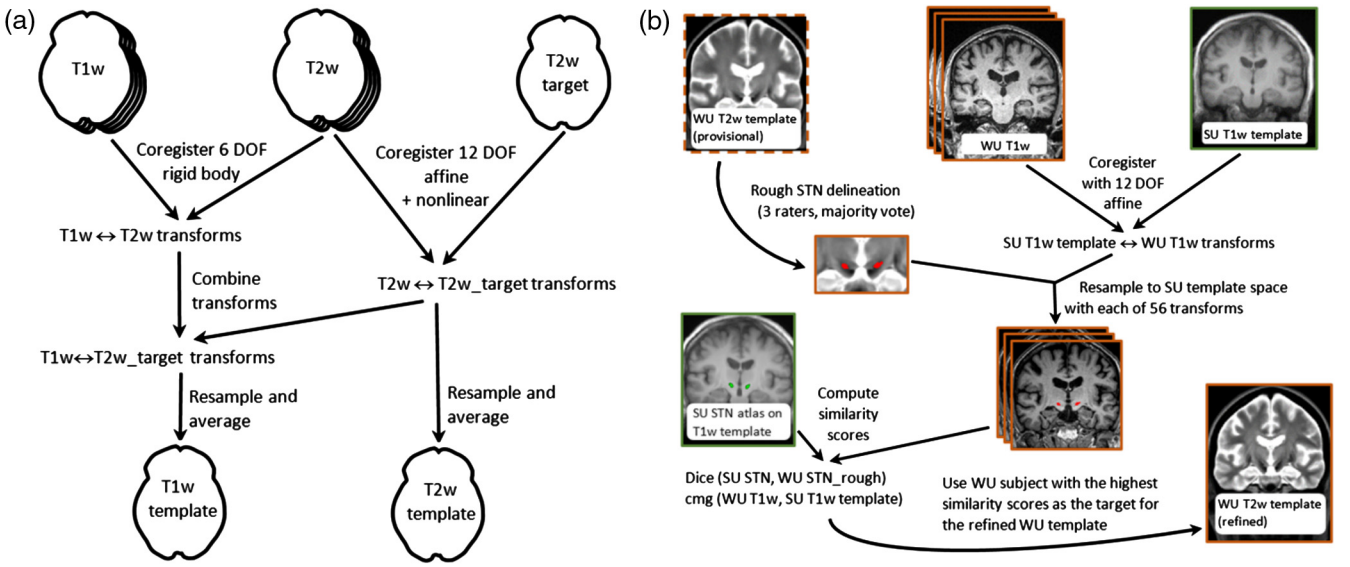

Fig. 1 Registration schemes used in average template creation. Arrows indicate information flow; image stacks represent iteration over all individuals in a given cohort. (a) Creating T1- and T2-weighted average templates. Both SU and WU templates were created according to this scheme. (b) Identifying WU participant for the registration target for refined WU templates. Orange indicates WU data, green indicates SU data.

Fig. 2 Creation of SU_7T_T2w_T template. (a) Triplanar view of registration target (SU_7T_T2w_t). (b) Averaged SU_7T_T2w_T template. Both images are in 7T data space. From left to right: coronal, axial, and sagittal (right hemisphere). Note well-matched anatomical detail achieved by *bm-cmg* and improved contrast to noise ratio. The cross-hair is centered on the right STN.

the selected target (SU_7T_T2w_t) was computed using *bm-cmg*. The warped T2w images then were intensity normalized to equate the mean voxel value over individuals and averaged to create the 7T T2-weighted template (SU_7T_T2w_T) [Figs. 1(a) and 2]. We computed a matching T1-weighted template (SU_3T_T1w_T) also by averaging T1w images warped to the T2w target by composition of transforms (i.e., T1w → T2w → SU_7T_T2w_t), followed by intensity normalization and averaging as for the T2w images. Thus, we created SU_7T_T2w_T and SU_3T_T1w_T (averaged T1- and T2-weighted template images), in SU data space, i.e., in register with SU_7T_T2w_t. The SU_3T_T1w_T template was very well matched to the SU_7T_T2w_t target image, the main difference being suppression of voxelwise noise (Fig. 2).

2.3.2 *Creating STN atlas from 7T images*

For each of the seven 7T participants, three experienced neuroanatomists delineated the left and right STN on T2w images (in native space) using FSLView.[26] STN boundaries were corrected for topological irregularities by removal of spikes and filling of holes. Spikes were defined as labeled voxels with two or less labeled neighbors in the immediate 6-voxel neighborhood and four or less labeled neighbors in the full 26-voxel neighborhood. Similarly, holes were defined as unlabeled voxels with three or more labeled voxels in the immediate neighborhood and 14 or more labeled voxels in the full neighborhood. Two iterations of topology correction were applied to each manually segmented STN region.

To evaluate consistency of delineations, the corrected labels (1 = STN; 0 = not STN) were compared across neuroanatomists using Dice coefficients. The Dice coefficient[27] is a standard measure of volume overlap used to compare manual segmentations [Appendix B(a)]. The average Dice coefficient over all STN delineations of the SU data was 0.65 with topology correction and 0.62 without (see Fig. 3 and Table 1). Dice coefficients tend toward low values for small structures and lower voxel resolution.[28] Therefore, we also evaluated the mean surface distance (*msd*)[29] [see Appendix B(b)], which provides

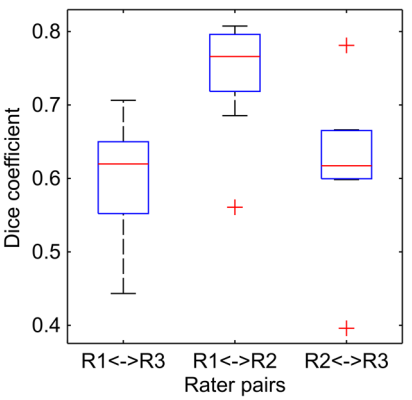

Fig. 3 Interrater agreement between raters R1, R2, and R3, delineating the STN in seven SU_7T_T2w images. The error bars denote ±2.7 standard deviations. Red "+" are outliers.

Table 1 Interrater Dice coefficient between bilateral STN delineations on SU 7T T2-weighted individual images, averaged over 7 SU participants. The three raters are R1, R2, and R3.

Raters	Dice, original	Dice, topology corrected
R1 ↔ R2	0.55	0.6
R1 ↔ R3	0.71	0.74
R2 ↔ R3	0.59	0.61

a complementary measure of segmentation consistency. The *msd* is computed as the average mismatch between surfaces of three-dimensional (3-D) segmentation masks. The *msd* over all STN delineations of the SU data was 0.58 mm.

A preliminary consensus STN segmentation was constructed by majority vote (all labels summed, then voxels below 2 discarded). These results (one label per participant bilaterally) then were warped to SU data space and summed. This summation generated an image with voxel values in the range [0 to 21]. Voxels having value less than or equal to 6 were discarded and the result was blurred with Gaussian kernel of 0.75 mm in each direction (FWHM of 1.3 mm in 3-D) and intensity scaled to produce STN "probabilistic" labels in the range [0.0 to 1.0] (Fig. 4).

2.4 *Creating Average 3T Template in the WU PD Cohort*

We created an average WU template in two stages, as detailed in subsequent sections. In brief, at the first stage, provisional T1w and T2w templates were created [Fig. 1(a)], and the STN was delineated on the T2w template. By applying the template → individual image transform, we obtained a rough provisional template-based STN delineation in each WU participant. At the second stage [Fig. 1(b)], each WU T1w patient's image was independently coregistered to the SU_3T_T1w_T template, and a provisional STN delineation was compared to the SU atlas-based delineation obtained in the previous section. Comparing provisional WU and SU STN delineations as well as evaluation of whole-brain cross-image similarity, determined the WU T1w patient best matching the SU template. This patient was used as the target to create the final (definitive) WU average T2w and T1w templates.

2.4.1 *Provisional WU templates*

The WU 3T T1-weighted and T2-weighted data were mutually coregistered following the scheme in Fig. 1(a). For each of the 56 patients, the T1w (MP-RAGE) and T2w (3D SPACE) images were coregistered by means of 6-DOF rigid body transforms. One patient with age-appropriate ventricular atrophy was provisionally selected to serve as the warp target (WU_3T_T2w_t) for the remaining 55 patients. The entire WU 3T T2-weighted and T1-weighted dataset was registered to the provisional target (WU_3T_T2w_t), intensity normalized and averaged (as for the SU data) to produce provisional 3T T2- and T1-weighted templates (WU_3T_T2w_T and WU_3T_T1w_T).

2.4.2 *Selecting WU target for the refined WU template*

The definitive 3T warp target was selected by identifying the patient anatomically most similar to the SU warp target (SU_7T_T2w_t), with anatomical similarity determined by Dice coefficient and *cmg* score as follows. First, the STN was roughly delineated in the provisional 3T template (WU_3T_T2w_T) by the same three raters (average Dice coefficient was 0.4), with majority vote delineation obtained as before. This delineation was transformed to each of WU T1w individual subject spaces. Second, each WU patient's T1-weighted image was 12-DOF affine transform registered to the SU_3T_T1w template [Fig. 1(b)]. Finally, each WU T1-weighted image, along with its rough STN delineation, was resampled to the SU_3T_T1w template space. This enabled us to compute for each WU patient: (1) the *cmg* objective function between T1w image and the SU T1w template, and (2) the Dice coefficient between rough WU STN delineation and SU 7T STN atlas. The patient with one of top five Dice scores and the highest *cmg* score was then selected as the definitive warp target to create the refined WU average template using the same registration scheme [Fig. 1(a)].

2.5 *Connecting the SU and WU Data Spaces*

We next applied *bm-cmg* to nonlinearly register the SU_3T_T1w_T and WU_3T_T1w_T templates. The resulting deformation field established the relation between the WU and SU data spaces. Alignment of SU_7T_T2w_T and WU_3T_T2w_T templates was verified visually by overlaying their edge maps (Fig. 5). Visual inspection of the 3T WU data in 7T SU data space indicated satisfactory alignment of brain boundaries, general gyral anatomy, and third and fourth ventricles. Additionally, the RN (clearly identifiable on both templates) was delineated on SU_7T_T2w_T and WU_3T_T2w_T and

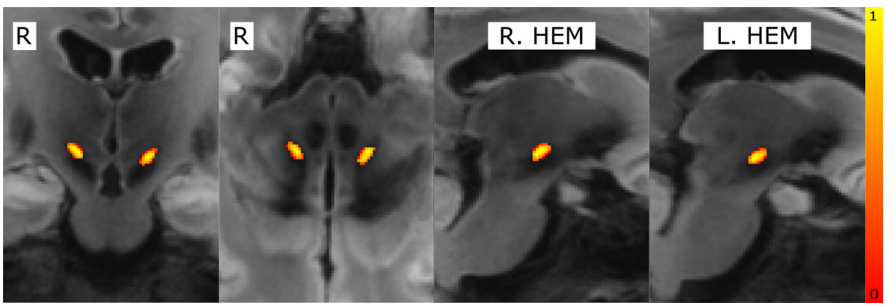

Fig. 4 Probabilistic representation of the STN in SU data space. From left to right: coronal, axial, sagittal (right hemisphere), and sagittal (left hemisphere).

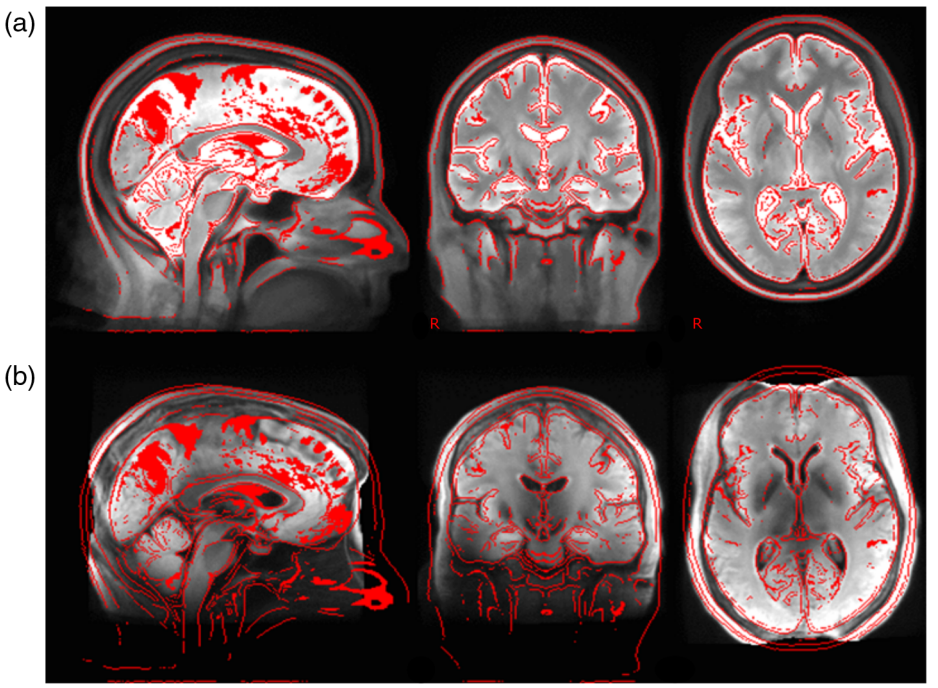

Fig. 5 (a) WU_3T_T2w_T averaged template. (b) SU_7T_T2w_T averaged template. From left to right: sagittal, coronal, and axial plane views. The red outlines are edge maps computed by FSL Slicer tool on the WU 3T template and duplicated on the SU 7T template. Note good match achieved by bm-cmg (whole-brain averaged alignment error = 1.3 mm).

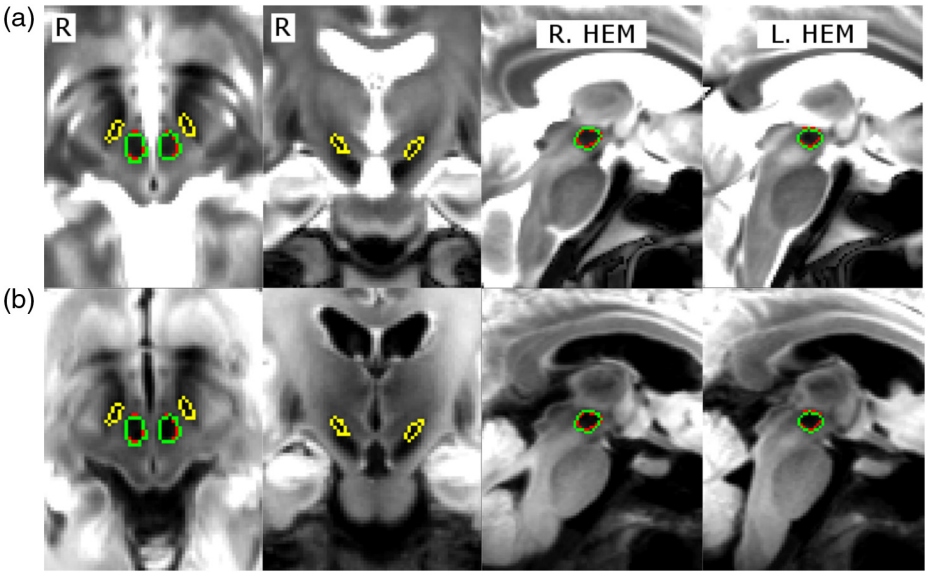

Fig. 6 Subcortical structures in WU data space. The following structures were delineated in SU space and resampled in WU space: STN (yellow) and RN (red). For comparison, RN was directly delineated on the WU_3T_T2_T template (green). (a) WU_3T_T2_T template; (b) SU_7T_T2_T template resampled in WU space. From left to right: axial, coronal, sagittal (right hemisphere), and sagittal (left hemisphere).

the RN segmentations were compared (Fig. 6). This comparison yielded a Dice coefficient of 0.87 and *msd* of 0.37 mm.

2.6 *Connecting the SU and WU Data to MNI152 Space*

Finally, the WU_3T_T1w_T template was aligned (12-parameter affine) to the MNI152_T1_0.5 mm average template (obtained via FSL 5.0) and the resulting transform was applied to the WU_3T_T2w_T template. Then, the WU_3T_T1w_T → MNI152_T1 transform was composed with the nonlinear SU → WU transform. The composed transform was applied to the SU_7T_T2w_T template to obtain WU 3T STN atlases in MNI152 space (Figs. 7 and 8). This STN "probabilistic" atlas, along with the SU_7T_T2w_T and 3T_T2w_T templates in MNI152 space, are publicly available in Ref. 30. The atlas is provided with

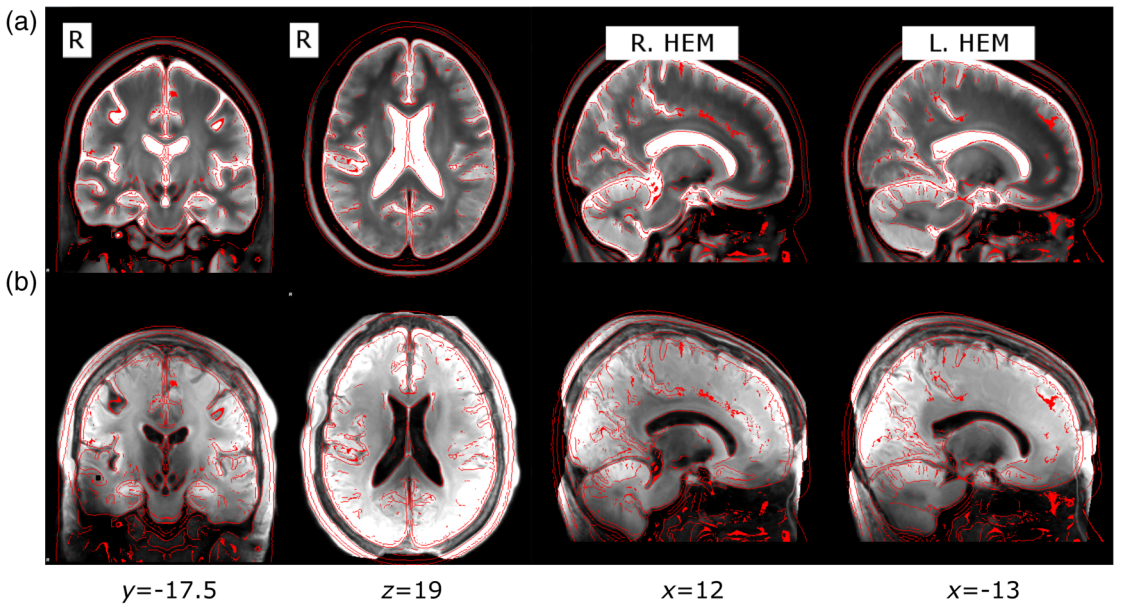

Fig. 7 (a) WU 3T and (b) SU 7T T2-weighted templates in MNI152 space. MNI152 plane coordinates are shown under each slice. Edge maps (red contours) were defined on the 3T template and duplicated on the 7T template.

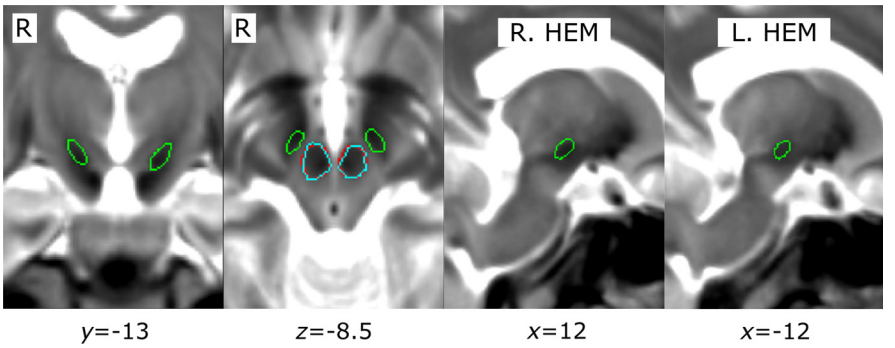

Fig. 8 Subcortical structures in MNI152 space. From left to right: coronal, axial, sagittal (right hemisphere), and sagittal (left hemisphere). MNI152 plane coordinates are shown under each slice. Green: STN originally delineated on the SU_7T_T2w_T template; blue: RN originally delineated on the SU_7T_T2w_T template; red: RN originally delineated on the WU_3T_T2w_T template.

binary STN labels, obtained by thresholding to match target volume as described in Appendix C. The same procedure can be used to create binary STN labels in any image space using this atlas.

3 Results

3.1 *Estimation of Error in the Nonlinear Registration of Individual WU 3T T2w Images to the WU_3T_T2_T Template*

Since all present transforms are invertible, an estimate of transform error can be obtained by composing any transform (affine or nonlinear) with its inverse. In theory, this composition generates the identity transform. In practice, deviation from the identity provides an estimate of computed transform error. Thus, the precision of alignment of individual T2w images to the WU_3T_T2w_T template by *bm-cmg* was estimated by computing the nonlinear T2w → WU_3T_T2w_T transform (see Sec. 2.3.2), then independently computing the inverse WU_3T_T2w_T → T2w transform and composing the results [see Appendix A(c) for details]. In this manner, we estimated the average across subjects of the misalignment between source and target images, expressed as a Euclidean distance at each voxel. We designate this quantity the voxelwise average alignment error (AAE). AAE maps were computed for each T2w image contributing to the WU_3T_T2w_T template. The mean AAE for the 56 T2w images aligned to WU_3T_T2w_T template was 1.3 mm evaluated over the whole brain. The same quantity evaluated over the STN was 0.62 ± 0.7 mm.

3.2 *Comparison to Previously Published Atlases*

We compared the present results to two other STN atlases. We first compared to an established, single-subject, histological atlas (Mai),[31] and then to a recently published basal ganglia atlas of 12 healthy control subjects based on high-definition 7T MRI (Wang).[17] To enable these comparisons, we registered

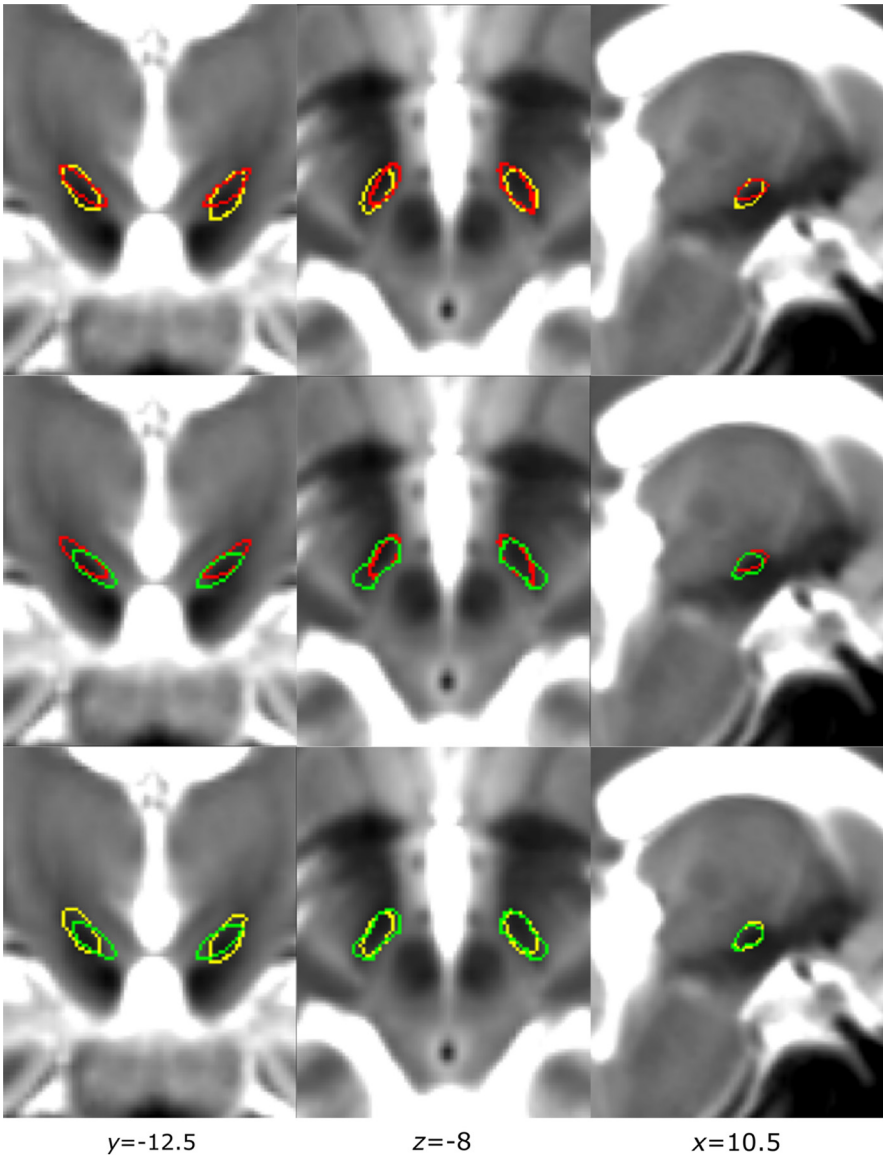

Fig. 9 Volume-matched STN boundaries defined in three atlases and represented in MNI152 space. The underlay is the WU_3T_T2w_T template in MNI152 space. Green: histologic atlas (Mai); yellow: current result; red: previously published 7T atlas (Wang). MNI152 plane coordinates are shown for each row. From left to right: coronal, axial, and sagittal (right hemisphere).

both of these alternative atlases to our WU_3T_T2w_T template, as described below.

3.2.1 *Coregistering to Mai atlas*

Since registering an MRI directly to a histological atlas is challenging, we coregistered our WU_3T_T2w_T template to an image set that was previously coregistered to the Mai histologic atlas. This dataset included clinical images acquired in a separate cohort of 84 PD patients undergoing DBS electrode implantation at WU, as described in Ref. 32. The dataset includes presurgical, full brain T2-weighted MRIs acquired with a Siemens Vision 1.5T scanner (TR 8.9 s, TE 0.09 s, flip angle 180 deg, magnetic field strength 1.5T, 1 mm × 2 mm × 2 mm voxels) and postoperative CT images (Siemens Somatom Plus 4 scanner, 0.5 mm × 0.5 mm × 2 mm voxels, 120 kV, 360 milli-Amp-sec). In comparing STN localizations obtained by the Mai atlas versus the present method, we duplicated the method of Videen et al. in which each patient's anatomy was registered to the Mai atlas via the postoperative CT. Thus, the Mai → CT transform was taken as a starting point. Registration of MRI data to the Mai atlas then proceeded as follows. First, the postsurgical CT was rigidly coregistered to the T2w MRIs of the same patient by optimizing *cmg*. Second, each T2w image was nonlinearly registered to the WU_3T_T2w_T template; the mean AAE of this operation was 0.71 mm evaluated over the STN. Finally, the Mai → WU_3T_T2w_T transform was obtained as Mai → CT → T2w → WU_3T_T2w_T.

3.2.2 *Coregistering to Wang atlas*

We also compared our method to the STN atlas of Wang et al.[17] We nonlinearly registered the WU_3T_T2w_T template to the Wang high-definition, T2-weighted 7T template (available in Ref. 33) using affine transformation followed by nonlinear *bm-cmg*.

3.2.3 *Atlas comparison results*

To enable an unbiased cross-atlas comparison, we transformed the image data to MNI152 0.5 mm isotropic voxel space using the same WU_3T_T2w_T → MNI152 linear transform described in Sec. 2.6. Transformed probabilistic structure masks (Fig. 9) were thresholded to match the volume of original STN labels in original space, as detailed in Appendix C. The resulting *msd*, Dice coefficient, and Euclidean distance between the centers of mass for all available structures are summarized in Table 2. Inspection of these results (Fig. 9) suggests comparable STN localization using either our new method or the atlas of Wang et al. Somewhat more discrepancy was apparent in comparisons involving the histologic (Mai) atlas.

4 Discussion

4.1 *Summary*

We present methodology for creating a high-definition, 3T probabilistic STN atlas derived from *in vivo* 7T MRI data.[23] We delineated the STN in 7T images in seven healthy individuals, then utilized a nonlinear registration method to create an average template derived from 7T images. This template then was nonlinearly coregistered to a 3T template representing the PD population. We then applied a volume preserving threshold to obtain a binary mask of the probabilistic STN. The 3T STN template enables localization of the STN in individuals with voxel-scale accuracy. We also aligned our 3T template to two other atlases and compared the resulting binary STN segmentations in a common space. We demonstrate high overlap of the STN with a publicly available 7T atlas and lower overlap using prior methodology based on a histological atlas.

4.2 *Limitations of Prior STN Atlases*

Localizing the STN in clinical MRI is challenging owing to the limited contrast provided by 1.5T or 3T scanners.[8] Inhomogeneous iron content of the STN[34,35] and small structure size contribute to this challenge. These difficulties can be addressed by localizing the STN using an appropriate atlas template. However, the accuracy of atlas-based localization in an individual depends on the quality of the atlas. A large proportion of human STN atlases currently in use was derived from *ex vivo* sections of a single brain.[11,31,32,36–41] The utility of such histological atlases is limited by out-of-plane distortions, in-plane tears, and inconsistent staining.[42] Moreover, the utility of single-subject atlases is limited by STN shape variability across individuals and age groups.[18,20–22] The present probabilistic atlas based on population averages of *in vivo* images avoids these limitations.

3T imaging has been used to create average STN atlases[12,28] that are well matched to the contrast properties of 3T scanners. Imaging at 7T provides better delineation of the STN. However, 7T scanners currently are not available in the clinical setting. Our approach combines STN delineation at 7T with template creation at 3T. Although this approach entails a rather elaborate, multimodal image registration scheme, we show that the average STN localization error attributable to nonlinear image registration is 0.71 mm, which is less than the voxel size of typical clinical images (0.9 mm).

The comparisons reported in Table 2 suggest that atlases derived from MRI (Ref. 17 and the present work) consistently localize the STN and RN with discrepancies on the order of 1 mm. Somewhat more discrepancy, on the order of 2 to 3 mm, was observed in comparisons to the method of Videen et al.,[32] which utilizes the histological atlas of Mai.[31] This greater discrepancy may reflect divergent contrast of subcortical structures in histological sections versus MRI. It is more likely that anatomical distortions owing to postmortem fixation are responsible. Additionally, the Mai atlas represents a 24-year old individual whereas the typical PD patient is considerably older, a key point since the STN shifts laterally with age.[18] This age-dependence is taken into account in the current work as well as in the probabilistic atlas of Wang et al.[17] Overall, our results suggest that MRI may be better suited for the construction of atlases intended to localize *in vivo* the STN in a clinical population. Additional studies are needed to investigate the extent to which such atlases are consistent. To facilitate this effort, we also made our atlas freely available to the research community. Ideally, these atlases should be compared using visualization tools, e.g., Ref. 43 and collated with DBS electrophysiology, diffusion MRI tractography, and *ex vivo* histology.

Table 2 Comparison of structures delineated in three atlases, resampled in MNI152 space. Comparison measures: (1) mean surface distance (*msd*), (2) Dice coefficient, and (3) Euclidean distance between the centers of mass (ΔCOM), reported separately for each side. "7T3T" refers to the current results.

Structure	Atlases	msd (mm)	Dice	ΔCOM left (mm)	ΔCOM right (mm)
STN	7T3T ↔ Wang	0.57	0.67	1.27	0.71
RN	7T3T ↔ Wang	0.35	0.83	0.42	0.31
STN	7T3T ↔ Mai	0.76	0.60	0.86	2.1
STN	Wang ↔ Mai	0.8	0.52	2.06	2.4

4.2.1 *bm-cmg*

Multimodal, nonlinear image registration is challenging.[44,45] Our initial attempts to compute nonlinear transforms using some available tools with default parameters[46–48] to coregister WU and SU datasets were not successful. Previously, we had an extensive experience with the *cmg* objective function for cross-modal affine registration, which has provided robust and reliable results in over 40 peer-reviewed publications within as well as outside our institution, e.g., Refs. 49 and 50. Since multiresolution block matching approach[45] was successfully used previously for coregistering deep brain structures (e.g., Yelnik, Bardinet[11]), we elected to combine this approach with *cmg* objective function in the *bm-cmg* algorithm. Combined with template refining strategy, this approach appeared to perform well in coregistering WU and SU datasets.

4.3 *Cross-Modal Coregistering of Different Patient Cohorts*

We hypothesized that if WU template registration target was anatomically close to the SU template image, higher nonlinear coregistration accuracy could be achieved. We then developed a strategy to select a subject from the WU cohort most similar to the SU template (Sec. 2.4), to serve as such target. This similarity was determined in two ways. First, each WU T1w image was linearly coregistered to the SU template, with higher value

of *cmg* objective function between the WU image and SU template identifying higher similarity. Second, we obtained approximate STN mask in each WU image using a provisional nonlinear T2w template. Although STN could not be identified directly on individual images, the provisional T2w template had enough contrast to make approximate delineation possible. The result was resampled to each subject's space by previously computed nonlinear transform. We then computed Dice scores between STN delineation on each individual WU image and SU template using the same linear transforms to resample.

5 Conclusions

We confirm that accurate delineation of STN is feasible using MRI acquired at 7T.[23] We extend this principle by creating a coregistered atlas representing 56 patients with PD scanned at 3T. The 3T atlas is suitable for localizing the STN in individuals with clinically available scanners. In particular, this atlas is intended for use in future studies targeting the STN with DBS electrodes. Technical advances developed in the course of this work include a nonlinear, multimodal registration technique (*bm-cmg*) and an approach to evaluate discrepancies in the localization of brain structures across different atlases.

Appendix A: Method for Nonlinear Multimodal Registration

a *cmg* Voxel Similarity Measure

The objective function is

$$\eta = \frac{\int |\nabla I_1||\nabla I_2|\cos^2\theta \mathrm{d}^3 r}{\int |\nabla I_1|\mathrm{d}^3 r \int |\nabla I_2|\mathrm{d}^3 r}, \tag{1}$$

where ∇I_1 and ∇I_2 are intensity gradients of images I_1 and I_2, $\cos\theta = (\nabla I_1 \Delta \nabla I_2)/|\nabla I_1||\nabla I_2|$, and integration spans over all voxels defined in both images. In the original description of the *cmg* voxel similarity measure, all registrations were effected by 12-parameter affine transforms.[24] The *cmg* is closely related to a previously described voxel similarity measure.[51]

b Nonlinear Alignment Method

Our nonlinear registration method employs multiscale block matching (*bm*) with Gaussian smoothing of median-filtered vector field obtained at different resolutions. This approach is similar to that described in Ref. 52, but uses the *cmg* measure as the objective function. *bm-cmg* starts by decomposing alignment source and target images into a multiscale pyramid with three levels. At each level, optimal local displacement is sought between blocks of integer voxel size that approximately match 8-mm isotropic cubes at the highest resolution. The displacement is estimated using a simplex method[53] with variable voxel step. The resulting deformation grid at the current scale is median filtered and smoothed with isotropic Gaussian kernel, initializing the optimization at the next scale.

bm-cmg was implemented in C++ using in-house image processing software libraries along with newmat[54] for matrix processing and simplex optimization implementation described in Ref. 53. The current implementation reads/writes images in 4dfp format compatible with Analyze 7.5 and FSLView.

c Estimation of Nonlinear Alignment Error at each Voxel

Let there exist a smooth isomorphic warp vector field $\hat{W}_{AB}$ from image A to image B, estimated at the center of each voxel by a computed approximation $\tilde{W}_{AB}$. Without the loss of generality, we can assume that both A and B are sampled in the same space and prealigned by an affine transform. For locus X_A in A, coordinates of matching loci $\tilde{X}_B$ and $\hat{X}_B$ in B can be expressed as

$$\tilde{X}_B = X_A + \tilde{W}_{AB}(X_A), \hat{X}_B = X_A + \hat{W}_{AB}(X_A), \tag{2}$$

where $\tilde{W}_{AB}(X_A)$ is the warp vector applied to X_A. Let also $\hat{W}_{BA} = \hat{W}_{AB}^{-1}$ be approximated by independently computed warp field $\tilde{W}_{BA}$. The error vector $\tilde{W}_{AB}$ of mapping X_A then can be defined as

$$E_{AB}(X_A) = \hat{X}_B - \tilde{X}_B = \hat{W}_{AB}(X_A) - \tilde{W}_{AB}(X_A). \tag{3}$$

Now, if we apply $\tilde{W}_{BA}$ to $\tilde{X}_B$, and denote the transform error as E_{BA}, we obtain from Eqs. (2) and (3), using Taylor series expansion of $\hat{W}_{BA}(\tilde{X}_B)$,

$$\mathrm{E}_{BA}(\tilde{X}_B) = \hat{W}_{BA}(\tilde{X}_B) - \tilde{W}_{BA}(\tilde{X}_B) \approx \hat{W}_{BA}(\hat{X}_B) - \mathrm{E}_{AB}(X_A) \circ \nabla\hat{W}_{AB} - \tilde{W}_{BA}(\tilde{X}_B), \tag{4}$$

where $\circ$ is the Schur (elementwise) product. Accordingly,

$$E_{AB}(X_A) + \mathrm{E}_{BA}(\tilde{X}_B) \approx -X_A - \mathrm{E}_{AB}(X_A) \circ \nabla\hat{W}_{AB} - \tilde{W}_{AB}(X_A) - \tilde{W}_{BA}(\tilde{X}_B). \tag{5}$$

Since the *bm-cmg* warp field gradient, $|\nabla\hat{W}_{AB}|$, is small, smooth, and slowly varying (with the average of 0.05 and maximum of 0.3 in our experiments), we can estimate the AAE for $\tilde{W}_{AB}$ and $\tilde{W}_{BA}$ by combining Eqs. (4) and (5).

$$|\mathrm{E}(X_A)| = \frac{1}{2}|\mathrm{E}_{AB}(X_A) + \mathrm{E}_{BA}(\tilde{X}_B)| \approx \frac{1}{2}|X_A + \tilde{W}_{AB}(X_A) + \tilde{W}_{BA}(\tilde{X}_B)|. \tag{6}$$

In other words, the AAE at locus X_A for independently computed warp fields $\tilde{W}_{AB}$ and $\tilde{W}_{BA}$ can be estimated from warping this locus to B and then back to A, and evaluating one half of the resulting displacement from the original position.

Appendix B: Comparison of Binary Labels

Dice Coefficient

For two binary masks L_1 and L_2, Dice coefficient[27] is computed as

$$D(L_1, L_2) = \frac{2|L_1 \cap L_2|}{|L_1| + |L_2|}. \tag{7}$$

Mean Surface Distance

Given a locus p and surface S, the Euclidean distance from p to S is defined as

$$d(p,S) = \min_{s \in S} d(p,s), \tag{8}$$

where d is unsigned Euclidean distance, s is a locus on S. Further, by surface $S(M)$ of a binary mask M without holes, we understand all labeled voxels with background voxels in the immediate neighborhood. Now consider two simply connected binary labels with surfaces S_1 and S_2. The mean distance md between S_1 and S_2[29] is computed as

$$md(S_1,S_2) = \frac{1}{|S_1|}\int_{S1} d(p,S_2)\mathrm{d}p, \tag{9}$$

where the surface distance from $p \in S_1$ to S_2 is averaged over all points in S_1. Symmetric version of this measure, referred to as mean surface distance (msd), is defined as

$$msd(S_1,S_2) = \frac{1}{2}[md(S_1,S_2) + md(S_2,S_1)]. \tag{10}$$

Appendix C: Thresholding Nonlinearly Transformed Labels to Match Target Volume

Defining structure boundaries in target image space requires binarization of resampled probabilistic structure labels. This operation potentially changes the volume of a structure, in our experience, by as much as 40%. To avoid this complication, the following iterative procedure was adopted to correctly choose the binarization threshold: (a) binarize the mask in the target space using an initial seed threshold value, (b) compute the volume of the inverse image of this label in the original space by integrating the transform's inverse Jacobian over the thresholded mask, and (c) adjust the threshold using a gradient descent strategy, targeting the volume in original (untransformed) space. Steps (a)–(c) are repeated until convergence is reached. The resulting binary mask thus always has the volume of the original mask scaled by the transform scale factor.

Appendix D: Expanded Methodological Details

1. Create SU 7T Average Template and Probabilistic STN Atlas.

   a. For all seven SU participants, coregister (6-parameter affine transform) the T1w and T2w images [Fig. 1(a)].

   b. Select, from among the 7 T2w images, the SU_7T_T2w target (SU_7T_T2w_t) according to following criteria:

      Low noise, artifact free T1w and T2w

      Normal ventricles

      Good STN contrast

   c. For the other six participants, compute the nonlinear transform (warp), T2w → SU_7T_T2w_t; compute, by composition of transforms, the corresponding T1w transform as T1w → T2w → SU_7T_T2w_t.

   d. For all seven participants, transform the T2w and T1w images to 7T target space.

   e. Scale the intensity of each transformed image to match average intensity across all seven images.

   f. Average the transformed images over the seven participants to create SU_3T_T1w_T and SU_7T_T2w_T average templates in SU target space [Fig. 1(a)].

   g. Delineate (using the three-rater, majority vote algorithm) the STN in the SU_7T_T2w_T average template.

2. Create WU 3T Average Template and Probabilistic STN Atlas in Register with the SU 7T Template.

   a. For all 56 WU patients, coregister (6-parameter affine transform, *cmg* objective function) the T1w and T2w images.

   b. Select a provisional WU_3T_T2w target (WU_3T_T2w_t) from the 56 patients according to following criteria:

      Low noise, artifact free T1w and T2w

      Normal ventricles

      No obvious asymmetries

   c. For the other 55 WU patients, compute the nonlinear transform, T2w → WU_3T_T2w_t; compute, by composition, the corresponding T1w transform as T1w → T2w → WU_3T_T2w_t.

   d. For all 56 WU patients, transform the 3T T2w and T1w images to WU target space.

   e. Average the transformed images over all 56 WU patients to create WU_3T_T1w_T and WU_3T_T2w_T average templates in WU target space.

   f. Delineate (using the three-rater, majority vote algorithm) the STN in the WU_3T_T2w_T average template; delineation is possible in the average owing to enhanced contrast to noise ratio.

   g. For all 56 WU patients, compute the 12-parameter affine transform, T1w → SU_3T_T1w_T by optimization of the *cmg* objective function. These results will be used later to select the patient with the definitive WU_3T_T2w_t.

   h. For all 56 WU patients, invert the (nonlinear) T2w → WU_3T_T2w_T transform to obtain WU_3T_T2w_T → T2w; compose transforms WU_3T_T2w_t → T2w → T1w → SU_3T_T1w_T to obtain WU_3T_T2w_t → SU_3T_T1w_T [Fig. 1(b)]; resample the WU STN delineation (obtained in step f) in SU_7T_target space.

   i. For all 56 WU patients, compute the Dice coefficient between the WU and SU STN delineations.

   j. Select the five patients with the highest Dice coefficient.

   k. Of these five patients, select the one with the greatest optimized (WU) T1w → SU_3T_T1w_T *cmg* objective function value (η) this 12-parameter affine transform was previously computed in step g.

The T2w of the selected patient becomes the definitive WU_3T_T2w target (WU_3T_T2W_t).

l. Compute the definitive WU average STN template by repeating steps (c–e).

m. Connect the WU and SU target spaces by computing the nonlinear WU_3T_T1w_T → SU_3T_T1w_T transform; transforms linking all WU and SU, T1w and T2w images, now are defined by transform composition.

Disclosures

The authors do not have relevant conflicts of interest to disclose.

Acknowledgments

Support for this work was provided by grants from the National Institute of Neurological Disorders and Stroke (NINDS), Award Nos. NS075321, NS41509, NS058714, NS097437, K23NS075097; and also from the Neuroimaging Informatics and Analysis Center (NIAC), Award No. 1P30NS098577. Additional support was provided by the Michael J. Fox Foundation; the Seiger Family Foundation; the Barnes Jewish Hospital Foundation (including the Elliot Stein Family Fund and Parkinson Disease Research Fund); the American Parkinson Disease Association (APDA) Advanced Research Center for Parkinson Disease at Washington University in St. Louis; the Greater St. Louis Chapter of the APDA; the Barbara & Sam Murphy Fund, and the Oertli Fund for Parkinson Disease Research.

References

1. A. Funkiewiez et al., "Long term effects of bilateral subthalamic nucleus stimulation on cognitive function, mood, and behaviour in Parkinson's disease," *J. Neurol. Neurosurg. Psychiatry* **75**(6), 834–839 (2004).
2. H. M. Smeding et al., "Neuropsychological effects of bilateral STN stimulation in Parkinson disease: a controlled study," *Neurology* **66**(12), 1830–1836 (2006).
3. J. M. Bronstein et al., "Deep brain stimulation for Parkinson disease: an expert consensus and review of key issues," *Arch. Neurol.* **68**(2), 165 (2011).
4. S. A. Eisenstein et al., "Acute changes in mood induced by subthalamic deep brain stimulation in Parkinson disease are modulated by psychiatric diagnosis," *Brain Stimul.* **7**(5), 701–708 (2014).
5. T. M. Ellis et al., "Reoperation for suboptimal outcomes after deep brain stimulation surgery," *Neurosurgery* **63**(4), 754–761 (2008).
6. M. S. Okun et al., "Management of referred deep brain stimulation failures: a retrospective analysis from 2 movement disorders centers," *Arch. Neurol.* **62**(8), 1250–1255 (2005).
7. M. S. Okun et al., "A case-based review of troubleshooting deep brain stimulator issues in movement and neuropsychiatric disorders," *Parkinsonism Relat. Disord.* **14**(7), 532–538 (2008).
8. S. F. Danish et al., "Conventional MRI is inadequate to delineate the relationship between the red nucleus and subthalamic nucleus in Parkinson's disease," *Stereotact. Funct. Neurosurg.* **84**(1), 12–18 (2006).
9. M. Shin et al., "Subthalamic nucleus stimulation in Parkinson's disease: postoperative CT-MRI fusion images confirm accuracy of electrode placement using intraoperative multi-unit recording," *Neurophysiol. Clin.* **37**(6), 457–466 (2007).
10. E. Bardinet et al., "A three-dimensional histological atlas of the human basal ganglia. II. Atlas deformation strategy and evaluation in deep brain stimulation for Parkinson disease," *J. Neurosurg.* **110**(2), 208–219 (2009).
11. J. Yelnik et al., "A three-dimensional, histological and deformable atlas of the human basal ganglia. I. Atlas construction based on immunohistochemical and MRI data," *NeuroImage* **34**, 618–638 (2007).
12. Y. Xiao et al., "Multi-contrast unbiased MRI atlas of a Parkinson's disease population," *Int. J. Comput. Assisted Radiol. Surg.* **10**, 329–341 (2015).
13. T. Liu et al., "Improved subthalamic nucleus depiction with quantitative susceptibility mapping," *Radiology* **269**, 216–223 (2013).
14. A. Schäfer et al., "Direct visualization of the subthalamic nucleus and its iron distribution using high-resolution susceptibility mapping," *Hum. Brain Mapping* **33**, 2831–2842 (2012).
15. Z.-H. Cho et al., "Direct visualization of deep brain stimulation targets in Parkinson disease with the use of 7-tesla magnetic resonance imaging," *J. Neurosurg.* **113**, 639–647 (2010).
16. L. A. Massey et al., "High resolution MR anatomy of the subthalamic nucleus: imaging at 9.4 T with histological validation," *NeuroImage* **59**, 2035–2044 (2012).
17. B. T. Wang et al., "Generation and evaluation of an ultra-high-field atlas with applications in DBS planning," *Proc. SPIE* **9784**, 97840H (2016).
18. M. C. Keuken et al., "Ultra-high 7T MRI of structural age-related changes of the subthalamic nucleus," *J. Neurosci.* **33**, 4896–4900 (2013).
19. M. Weiss et al., "Spatial normalization of ultrahigh resolution 7 T magnetic resonance imaging data of the postmortem human subthalamic nucleus: a multistage approach," *Brain Struct. Funct.* **220**, 1695–1703 (2015).
20. M. C. Keuken et al., "Quantifying inter-individual anatomical variability in the subcortex using 7 T structural MRI," *NeuroImage* **94**, 40–46 (2014).
21. Y. Xiao et al., "Investigation of morphometric variability of subthalamic nucleus, red nucleus, and substantia nigra in advanced Parkinson's disease patients using automatic segmentation and PCA-based analysis," *Hum. Brain Mapp.* **35**(9), 4330–4344 (2014).
22. J. Rong et al., "A new atlas localization approach for subthalamic nucleus utilizing chinese visible human head datasets," *PLoS ONE* **8**(2), e57264 (2013).
23. M. Saranathan et al., "Optimization of magnetization-prepared 3-dimensional fluid attenuated inversion recovery imaging for lesion detection at 7 T," *Invest. Radiol.* **49**(5), 290–298 (2014).
24. D. J. Rowland et al., "Registration of [^{18}F]FDG microPET and small-animal MRI," *Nucl. Med. Biol.* **32**, 567–572 (2005).
25. S. Yousefi, N. Kehtarnavaz, and A. Gholipour, "Improved labeling of subcortical brain structures in atlas-based segmentation of magnetic resonance images," *IEEE Trans. Biomed. Eng.* **59**(7), 1808–1817 (2012).
26. M. Jenkinson et al., "Fsl," *Neuroimage* **62**(2), 782–790 (2012).
27. L. R. Dice, "Measures of the amount of ecologic association between species," *Ecology* **26**(3), 297–302 (1945).
28. C. Haegelen et al., "Automated segmentation of basal ganglia and deep brain structures in MRI of Parkinson's disease," *Int. J. Comput. Assisted Radiol. Surg.* **8**, 99–110 (2013).
29. P. Cignoni, C. Rocchini, and R. Scopigno, "Metro: measuring error on simplified surfaces," *Comput. Graphics Forum* **17**, 167–174 (1998).
30. M. Milchenko, "7T probabilistic atlas of subthalamic nucleus for use with 3T MRI," 2017 https://www.nitrc.org/projects/stn7t3t/.
31. J. Mai, J. Assheuer, and G. Paxinos, *Atlas of the Human Brain*, 2nd ed., Academic Press, San Diego, California (2004).
32. T. O. Videen et al., "Validation of a fiducial-based atlas localization method for deep brain stimulation contacts in the area of the subthalamic nucleus," *J. Neurosci. Methods* **168**, 275–281 (2008).
33. J. Lau and A. Khan, "Ultra-high field atlas for DBS planning," https://www.nitrc.org/projects/deepbrain7t (28 July 2017).
34. M. Azuma et al., "Lateral asymmetry and spatial difference of iron deposition in the substantia nigra of patients with Parkinson disease measured with quantitative susceptibility mapping," *Am. J. Neuroradiol.* **37**, 782–788 (2016).
35. G. de Hollander et al., "A gradual increase of iron toward the medial-inferior tip of the subthalamic nucleus," *Hum. Brain Mapp.* **35**, 4440–4449 (2014).
36. A. F. Sadikot et al., "Creation of computerized 3D MRI-integrated atlases of the human basal ganglia and thalamus," *Front. Syst. Neurosci.* **5**, 71 (2011).
37. N. Nakano et al., "Computed three-dimensional atlas of subthalamic nucleus and its adjacent structures for deep brain stimulation in Parkinson's disease," *ISRN Neurol.* **2012**, 1–13 (2012).

38. A. Sudhyadhom et al., "A three-dimensional deformable brain atlas for DBS targeting. I. Methodology for atlas creation and artifact reduction," *Open Neuroimage J.* **6**, 92–98 (2012).
39. G. Schaltenbrand and W. Wahren, *Atlas for Stereotaxy of the Human Brain*, Thieme, Stuttgart (1977).
40. J. Talairach and P. Tournoux, *Co-Planar Stereotaxic Atlas of the Human Brain*, Thieme, Stuttgart (1988).
41. M. M. Chakravarty et al., "The creation of a brain atlas for image guided neurosurgery using serial histological data," *Neuroimage* **30**(2), 359–376 (2006).
42. W. L. Nowinski, J. Liu, and A. Thirunavuukarasuu, "Quantification and visualization of the three-dimensional inconsistency of the subthalamic nucleus in the Schaltenbrand-Wahren brain atlas," *Stereotact. Funct. Neurosurg.* **84**(1), 46–55 (2006).
43. A. Horn and A. A. Kühn, "Lead-DBS: a toolbox for deep brain stimulation electrode localizations and visualizations," *NeuroImage* **107**, 127–135 (2015).
44. M. A. Viergever et al., "A survey of medical image registration—under review," *Med. Image Anal.* **33**, 140–144 (2016).
45. A. Sotiras, C. Davatzikos, and N. Paragios, "Deformable medical image registration: a survey," *IEEE Trans. Med. Imaging* **32**(7), 1153–1190 (2013).
46. M. Jenkinson et al., "Improved optimization for the robust and accurate linear registration and motion correction of brain images," *NeuroImage* **17**, 825–841 (2002).
47. J. L. R. Andersson, M. Jenkinson, and S. Smith, "Non-linear registration aka spatial normalisation," FMRIB Technical Report, FMRIB Centre, Oxford, United Kingdom (2007).
48. M. Modat, "Efficient dense non-rigid registration using the free-form deformation framework," Doctoral Thesis, University College London (2012).
49. L. L. Dugan et al., "Carboxyfullerene neuroprotection postinjury in Parkinsonian nonhuman primates," *Ann. Neurol.* **76**(3), 393–402 (2014).
50. M. V. Milchenko et al., "Comparison of perfusion-and diffusion-weighted imaging parameters in brain tumor studies processed using different software platforms," *Acad. Radiol.* **21**(10), 1294–1303 (2014).
51. J. P. Pluim, J. B. Maintz, and M. A. Viergever, "Image registration by maximization of combined mutual information and gradient information," *IEEE Trans. Med. Imaging* **19**, 809–814 (2000).
52. Y. H. Lau, M. Braun, and B. F. Hutton, "Non-rigid image registration using a median-filtered coarse-to-fine displacement field and a symmetric correlation ratio," *Phys. Med. Biol.* **46**, 1297–1319 (2001).
53. W. H. Press et al., *Numerical Recipes 3rd Edition: The Art of Scientific Computing*, Sample Page from Numberical Recipes in C, Vol. **1**, p. 506, Cambridge University Press, Cambridge, United Kingdom (2007).
54. R. B. Davies, "Writing a matrix package in C++," in *OON-SKI94*, pp. 207–213 (1994).

Mikhail Milchenko received his MS degree in mathematics from Lomonosov Moscow State University in 1999, and his PhD in computer science from Louisiana State University in 2005. He currently works as a research instructor at Washington Unversity's Mallickrodt Institute of Radiology. His research involves various aspects of medical image analysis, with particular interest lying in numerical optimization and machine learning techniques applied to image registration, implant detection, and cancer management.

Scott A. Norris is an assistant professor of neurology at Washington University. He received his MD degree from the University of Missouri-Columbia in 2008, then completed a neurology residency and movement disorders fellowship at Washington University. His current research interests include application of functional neuroimaging techniques in movement disorders, including dystonia, Parkinson disease, and essential tremor. He sees patients in the Movement Disorders Clinic and is involved in patient selection and management of patients undergoing DBS surgery.

Kathleen Poston is an associate professor of neurology and neurological sciences and (by courtesy) neurosurgery at Stanford University. She received her bachelor's degree of science in bioengineering from the University of Pennsylvania, her master's degree in biomedical engineering, and her MD degree from Vanderbilt University. She completed her neurology residency training at UCSF. She also completed a fellowship in clinical movement disorders at Columbia University and post-doctoral research training in functional neuroimaging at Feinstein Institute.

Meghan C. Campbell received her PhD in clinical science from Indiana University. She is an associate professor in neurology and radiology at Washington University in St. Louis. Her research interests include the neuropsychology of Parkinson disease, effects of treatment on cognition and mood in Parkinson disease, and identification of prognostic biomarkers for Parkinson disease.

Mwiza Ushe completed his MA degree in neuroscience and MD degree in Washington University in St. Louis in 2007. He finished his residency in neurology in 2011 and fellowship in movement disorders in 2013 at Washington University. He is currently a movement disorders specialist directing the Deep Brain Stimulation Program at Washington University. His research interests include the surgical management of movement disorders, mechanisms of DBS, and kinematics.

Joel S. Perlmutter is the Stein family professor of neurology, professor of radiology, neuroscience, occupational therapy, and physical therapy at Washington University. He heads movement disorders, the APDA Advanced Research Center, and the HDSA Center of Excellence. He serves on the Scientific Advisory Board of the APDA, the Dystonia Medical Research Foundation, cochairs the Scientific Advisory Committee of the Parkinson Study Group, and chairs the Standards Committee of the Huntington Study Group.

Abraham Z. Snyder is the professor of radiology at Washington University. He earned his PhD from Rockefeller Univerisity, and MD degree from the State University of New York at Buffalo School of Medicine. His work consists of applied image processing, involving functional and structural magnetic resonance imaging as well as metabolic and receptor imaging using positron emission tomography.